Effects of Shock-Induced Separation on Boundary Layer Transitional Mechanisms

Nikhil Mahalingesh, Sébastien Piponniau, Pierre Dupont

Effects of Shock-Induced Separation on Boundary Layer Transitional Mechanisms

Nikhil Mahalingesh*, Sébastien Piponniau† and Pierre Dupont‡
Aix Marseille Univ, CNRS, IUSTI, Marseille, France

The transitional mechanisms of a natural boundary layer as well as one interacting with shock-waves are investigated at supersonic speeds. Experiments are performed over a flat plate and a 6° compression ramp at a Mach number of 1.65, using Pitot probes and hot-wire anemometry. Comparisons are drawn between the two configurations focusing on the evolution of unstable modes of the boundary layer. Measurements are made inside the laminar boundary layer to study the primary and secondary instabilities of the natural transition process. While the flat plate exhibits the classical mechanisms of transition for a zero pressure gradient boundary layer, the compression ramp shows an altered transition process where the secondary instabilities play a less important role.

I. Nomenclature

c_f	=	Skin-friction coefficient
c_p	=	Pressure coefficient
δ_{99}	=	Boundary layer thickness $[m]$
δ^*	=	Compressible displacement thickness $[m]$
$\overline{e}$	=	Mean voltage of the hot-wire probe $[V]$
f	=	Frequency $[Hz]$
H_i	=	Incompressible shape factor
L_{int}	=	Length of interaction $[m]$
M	=	Mach number
n	=	Non-dimensional amplitude
ω^*	=	Non-dimensional angular frequency
p	=	Static pressure $[Pa]$
q	=	Dynamic pressure $[Pa]$
Re_{δ^*}	=	Reynolds number based on the compressible displacement thickness
Re_u	=	Unit Reynolds number $[m^{-1}]$
Re_x	=	Reynolds number based on the stream-wise coordinate
$(\rho U)'/(\overline{\rho U})$	=	Non-dimensional fluctuations of mass-flux
St_L	=	Strouhal number based on the length of interaction
σ_x	=	Band-passed standard deviation at a location x
σ_0	=	Band-passed standard deviation at the free-stream of the wind tunnel
U_∞	=	Free-stream velocity $[m/s]$
u_e	=	External velocity outside the boundary layer $[m/s]$
X^*	=	Non-dimensional stream-wise coordinate

II. Introduction

The transitional mechanisms of laminar boundary layers have been an important field of study for many decades in the discipline of aerodynamics [1]. Understanding this flow phenomenon is of great importance due to the significant advantage of lower skin-friction drag associated with laminar boundary layers, especially at supersonic and hypersonic

*PhD Student, nikhil.mahalingesh@univ-amu.fr.
†Associate Professor, sebastien.piponniau@univ-amu.fr.
‡Senior Researcher, pierre.dupont@univ-amu.fr.

speeds. Further, wall-heat fluxes from a transitioning boundary layer at very high speeds may be larger than even those encountered with turbulent boundary layers [2]. Consequently, laminar-to-turbulent transition has been extensively studied from theoretical [3, 4], experimental [5, 6] and numerical [7] points of view, with the first studies as far back as the early 20th century [8]. The classical self-excited Tollmien–Schlichting (TS) waves of incompressible boundary layers become three-dimensional at supersonic speeds (i.e. oriented with an angle with respect to the stream-wise direction) and hence are referred to as oblique modes [9]. At low supersonic speeds, the preferred scenario for transition involves the breakdown of stream-wise streak-like structures created by the non-linear interaction of oblique modes [10]. It was found that pairs of oppositely oriented oblique waves generate rapidly growing stream-wise structures [11]. These highly unstable streaks breakdown locally to create turbulent spots, leading to turbulence [12]. At hypersonic speeds, "Mack" modes are the most dominant characterized by very high frequencies [3]. This transition scenario is quite different from the breakdown process followed by the growth of oblique modes and streaks. Although extensive research has been carried out on both the oblique modes and the streak-like structures, including characterizing their spatial and temporal dynamics, their effects and influence on the length and time-scales of various other flow phenomena involving laminar boundary layers are still not well understood.

One such flow phenomenon is the interaction of boundary layers with shock-waves. Shock-wave boundary layer interaction (SBLI) is a classical flow phenomenon of high speed aerodynamics. SBLIs are encountered in various applications such as engine inlets, transonic wings, rocket nozzles, high-speed compressors, etc. and hence, this topic has received a lot of attention over the past 70 years [13, 14]. When the shock strengths are high, the interaction tends to separate the boundary layer and a characteristic length of separation is obtained [15]. This length of interaction was found to scale non-linearly with shock strength, Reynolds and Mach number, with further dependence on the type of flow geometry such as oblique shock reflections and compression ramps [16]. Further, such interactions are typically associated with intense low-frequency oscillations of shock-waves and large-scale "breathing" of the separation bubble [17, 18]. The mechanism of this unsteadiness has been the subject of much debate, where the scientific community was divided on the origins of this low-frequency dynamics, between the upstream boundary layer and downstream separated region [19, 20]. It has to be noted that most of these studies were extensively focused on turbulent SBLIs and relatively less attention has been given to the interaction of laminar boundary layers with shock-waves [21, 22].

Recent interest in transitional interactions sought to characterize and establish an experimental and numerical database for various flow parameters and geometries [23]. These studies found a strong correlation between the location of boundary layer transition and the size of the separated region [24]. Additionally, a discrepancy was found in the frequency of large-scale unsteadiness between experimental and numerical studies [25, 26]. Detailed investigations into the dynamics of transitional SBLIs showed that low-frequency unsteadiness may be directly influenced by the breakdown of coherent structures at reattachment [27]. Further, Large Eddy Simulations (LES) of transitional SBLIs found that the amplitude of low-frequency unsteadiness varied significantly with the size of the separated region, which in turn was dependent on the amplitude of initial disturbances in the incoming boundary layer [26]. On the experimental side, high-resolution Laser Doppler Anemometry (LDA) and hot-wire measurements showed that specific frequency scales are exponentially amplified over the interaction, reaching a maximum at the location of transition, suggesting that they might be related to boundary layer transitional mechanisms [28]. However, these experiments could not characterize the exact mechanism of transition over the SBLI and required further studies to complete the picture.

The current paper hopes to advance the collective knowledge on the transitional mechanisms of supersonic laminar boundary layers. In particular, the paper focuses on the differences between the natural transition process over a flat plate and the accelerated transitional mechanisms over a compression ramp. The following section details the experiments that used high-resolution hot-wire anemometry as the primary diagnostic tool. The results of the natural boundary layer are discussed first and followed by the compression ramp experiments. The current paper focuses on the mechanism of transition and the associated differences between the two geometries.

III. Experimental Methodology

The experimental facilities of the supersonic wind tunnel at the IUSTI laboratory of Aix-Marseille University are used for performing the measurements. It is a closed-circuit continuous-operation wind tunnel with hypo-turbulent free-stream conditions. Experiments can be conducted up to 4 hours with nearly constant operating conditions. A classical converging-diverging nozzle accelerates the flow to a Mach number of 1.65 and a free-stream velocity of 464 m/s. The total pressure of the free-stream was set to 0.8 atm, with a total temperature of 305 K, resulting in a unit Reynolds number of 11.01 million m^{-1}. Turbulence intensity of 0.05% in terms of mass-flux fluctuations, 0.03% in terms of velocity fluctuations and 0.11% in terms of pressure fluctuations, was measured using hot-wire anemometry at

the exit of the nozzle. Such low values of turbulence intensities are necessary to avoid bypass transition of the laminar boundary layers [29]. Downstream of the nozzle, the test section has a height of 105 mm and span-wise width of 170 mm.

The two geometrical configurations of the flat plate and the compression ramp are similar in design and construction. Both have a sharp leading edge and a thickness of 5 mm, placed at a height of 25 mm from the floor of the test section. The picture and schematic of the flat plate geometry is shown in Fig. 1. The compression ramp has a 6° deflection at 115 mm from the leading edge as shown in Fig. 2.

(a) Picture of the flat plate.

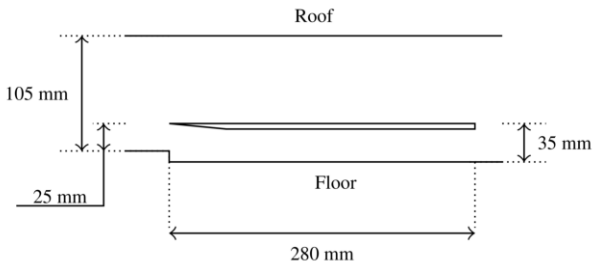

(b) Schematic of the flat plate.

Fig. 1 Flat plate geometrical configuration.

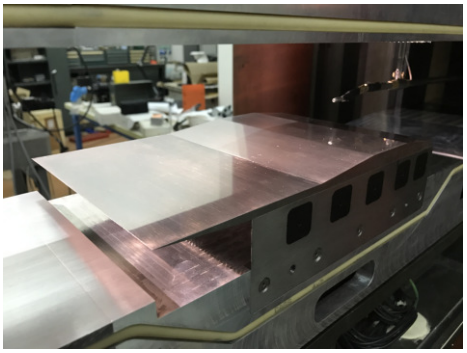

(a) Picture of the compression ramp.

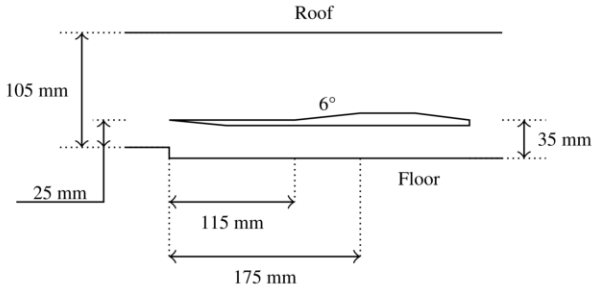

(b) Schematic of the compression ramp.

Fig. 2 Compression ramp geometrical configuration.

A supersonic Pitot probe, with a flat tip of 0.3 mm in height with a pressure tap of 0.15 mm, is used for measurements of mean flow quantities. The probe is traversed every 0.05 mm in the wall-normal direction to obtain boundary layer profiles, and longitudinal exploration over the compression ramp are made at a height of 5 mm from the wall. Isentropic compressible flow equations and normal shock relations are applied to the Pitot measurements and steady-state flow quantities are obtained.

A hot-wire anemometer setup with a tungsten and platinum wire of 2.5 μm diameter is used with Dantec Dynamics' Streamline amplifier. The anemometer is operated in constant temperature mode with a symmetrical bridge. The overheat ratio is set to 0.8 and the effective frequency bandwidth is approximately 150 kHz (depending on the wire characteristics). Measurements are sampled at 400 kHz for 10 seconds using the National Instruments NI6133 acquisition system with 14 bits of resolution.

Boundary layer hot-wire probes are used for measurements at the wall (Fig. 3b). A number of studies have shown that such probes can be placed inside laminar boundary layers to obtain reliable measurements , and even at supersonic flow conditions [1, 5, 6]. A small resin at the corner of the prongs is applied so that they can be placed flush on the wall while resting on the resin. This is to ensure the vibrations and oscillations of the probe and its support system are damped.

(a) External hot-wire prongs. **(b) Boundary layer hot-wire prongs.**

Fig. 3 Pictures of the two types of hot-wire prongs.

Figure 4 illustrates the measurement points made inside the laminar boundary layer, where the wire was at a constant wall-normal distance of 0.4 mm from the wall. From the illustration, it can be seen that the boundary layer thickness is lower than 0.5 mm over the first half of the flat plate. As a result, boundary layer measurements could not be performed here as the probe was outside or close to the edge of the boundary layer.

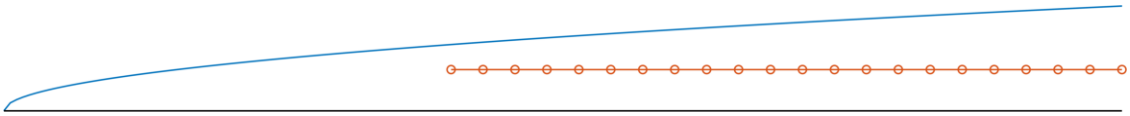

Fig. 4 Illustration of the hot-wire measurements made inside the boundary layer.

However, hot-wire probes cannot be placed inside separated regions with reverse flow as the wire cannot distinguish between positive and negative velocities, and furthermore, the wire is easily broken. Hence, classical flat hot-wire probes are traversed over the SBLI (Fig. 3a). The probe in the external flow is sensitive to fluctuations radiated by the boundary layer and associated flow structures of the interaction [30, 31]. Additionally, fluctuations from the flow on the side walls and the roof of the test section also influence the hot-wire measurements, but the amplitude of these "artifacts" decay rapidly moving away from their respective sources. Given the large size of the test section (relative to the boundary layer thickness on the side walls and roof), a probe placed in the mid-span and close to the laminar boundary layer has minimal influence from these artifacts. The instantaneous voltage of the hot-wire is influenced by fluctuations of total temperature, mass-flux and Mach number of the flow. For Mach numbers higher than 1.4 and high overheat ratios, non-dimensional fluctuations of mass-flux can be directly obtained from the hot-wire measurements using the King's law coefficient [32, 33]. Information regarding the time-scales of the boundary layer and the interaction can thus be obtained from the measurements of the hot-wire anemometer. Fourier analyses are applied to the measured time-signals and estimates of Power Spectral Density (PSD) are determined using Welch's method. Frequencies up to 200 kHz are resolved and fully converged spectral statistics are obtained with 2^{16} discrete Fourier points.

IV. Results

The first part of the results section focuses on the measurements over the flat plate and the second part details the results of the compression ramp.

A. Natural Boundary Layer

Measurements of the boundary layer profile at different stream-wise locations on the flat plate are shown in Fig. 5. The profiles are represented in similarity coordinates, where non-dimensional wall-normal distance is shown on the horizontal axis, scaled with respect to the boundary layer thickness (δ_{99}) and non-dimensional velocity is shown on the vertical axis, scaled with respect to the external velocity outside the boundary layer (u_e). The measurements are compared with the compressible Blasius and turbulent boundary layer profiles, which are obtained numerically for the Mach and Reynolds number of the current experiments. The stream-wise coordinate is expressed in terms of Reynolds number based on the compressible boundary layer thickness (Re_{δ^*}), which considers compressibility and

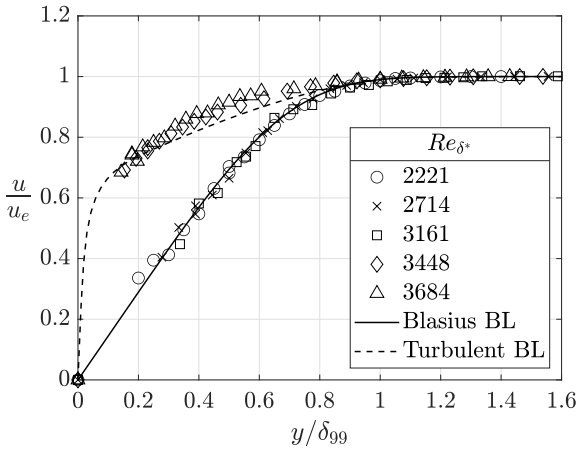

Fig. 5 Boundary Layer velocity profiles at different Reynolds numbers.

Mach effects. Such a scaling parameter has been previously used to study transitional laminar boundary layers [3, 5]. At low Reynolds numbers, the measured profiles exhibit a large linear behavior near the wall, characteristic of laminar boundary layers. Comparisons with theoretical Blasius profiles yield good agreements. However, at higher Reynolds numbers, the measurements deviate significantly from the Blasius profile and are closer to the turbulent profile.

Table 1 Incompressible shape factor of boundary layer profiles.

Re_{δ^*}	H_i
Blasius	2.69
2221	2.64
2714	2.83
3161	2.70
3448	2.13
3684	2.10
Turbulent	1.42

To understand the state of the boundary layer in more detail, table 1 shows the incompressible shape factor (H_i) of the profiles, and comparisons are drawn with theoretical shape factors for laminar and turbulent boundary layers. The shape factor at lower Reynolds numbers are close to the Blasius profile, but it reduces significantly at higher Reynolds numbers, but does not reach the shape factor of a fully turbulent profile. This suggests that the boundary layer is still in its transitional stages. It is to be noted that the lack of measurement points close to the wall has an influence on the calculated shape factor. Nevertheless, these results suggest that the beginning of transition significantly changes the boundary layer profile, making it "fuller".

Moving to the time-scales of the boundary layer, Fig. 6 shows the contours of PSD at different stream-wise locations on the flat plate. The PSD is represented in pre-multiplied and normalized format to highlight the dominant frequencies at each stream-wise location. Non-dimensional angular frequency (ω^*) is shown on the vertical axis in logarithmic scale. Frequency is normalized according to Eq. 1, where U_∞ is the free-stream velocity and Re_u is the unit Reynolds number of the free-stream. This normalization is typically used to identify boundary layer modes [3].

$$\omega^* = \frac{2\pi f}{U_\infty Re_u} \tag{1}$$

The contour map on the bottom corresponds to the measurements made inside the boundary layer (Fig. 4) and the one on the top corresponds to measurements made outside the boundary layer at a constant height of 3.85 mm from the wall. Inside the boundary layer, two time-scales are most dominant. At lower Reynolds numbers, the PSD is concentrated at high frequencies (HF) around $2 \times 10^{-5} \leq \omega^* \leq 4 \times 10^{-5}$. These scales are typically associated with the

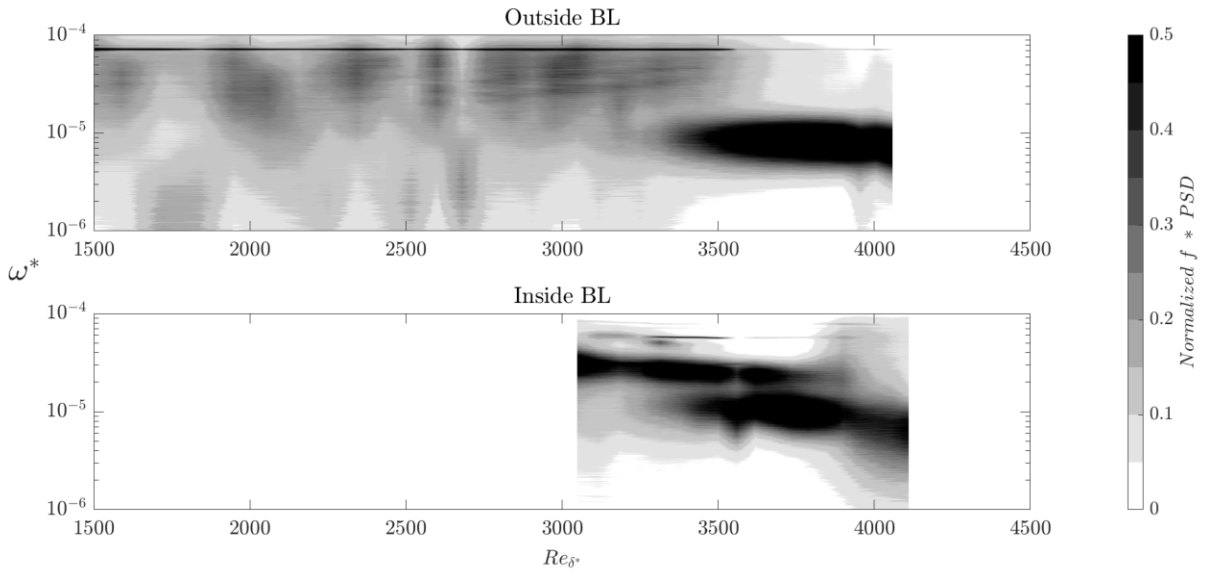

Fig. 6 Stream-wise evolution of normalized pre-multiplied power spectral density of the laminar boundary layer.

compressible version of Tollmien–Schlichting (TS) waves, which are 3D and oblique in nature for supersonic boundary layers [5, 6]. According to stability theory, these scales are the natural eigen modes of the boundary layer, arising due to the linear growth of small disturbances [3]. These oblique modes have been documented extensively by numerical and experimental studies [9, 10, 34, 35].

Further downstream on the plate, a medium frequency (MF) scale around $4 \times 10^{-6} \leq \omega^* \leq 2 \times 10^{-5}$, appears alongside the HF scale. These scales are characteristic of stream-wise streak-like structures associated with the non-linear stage of the transition process [7]. These scales are created when the amplitude of the oblique modes reach a certain threshold, triggering the formation of secondary scales [36, 37]. The presence of these scales indicate the beginning of the non-linear regime of the transition process, which is soon followed by breakdown and turbulence [12].

Outside the boundary layer, the hot-wire probe picks up radiated fluctuations from the boundary layer. It can be seen that for the beginning of the flat plate, the hot-wire records mostly the noise of the wind tunnel. No coherent frequency scale can be observed and relatively low energy is spread over a broad range of high frequencies. However, near the end of the flat plate, a clear time-scale can be observed corresponding to the MF scale seen inside the boundary layer. It seems that the HF scale observed inside the boundary layer is not seen outside, only the MF scales are observed at roughly the same location as seen inside. These results suggest that the HF oblique modes do not radiate fluctuations outside the boundary layer unlike the MF streak-like structures.

To shed light on the growth rates of these scales, Fig. 7 shows the non-dimensional amplitude of mass-flux fluctuations along the flat plate, from the hot-wire measurements. The PSD is integrated over a short band of frequencies associated with the two time-scales of interest to obtain band-passed standard deviation (σ_x), according to Eq. 2, where $\overline{e}$ is the mean voltage of the hot-wire probe. The band-passed standard deviation at each location is compared with the noise of the wind tunnel (σ_0) over the same band of frequencies to obtain non-dimensional amplitude (n), as shown in Eq. 3). The noise of the wind tunnel is measured at the exit of the converging-diverging nozzle and serves as the input to the laminar boundary layer. This normalization helps distinguish the presence of coherent time-scales associated with the boundary layer from the wind tunnel noise and the electronic noise of the hot-wire system.

$$\sigma_x = \sqrt{\int_{f_1}^{f_2} \frac{PSD}{(\overline{e})^2} df} \tag{2}$$

$$n = \frac{\sigma_x}{\sigma_0} \tag{3}$$

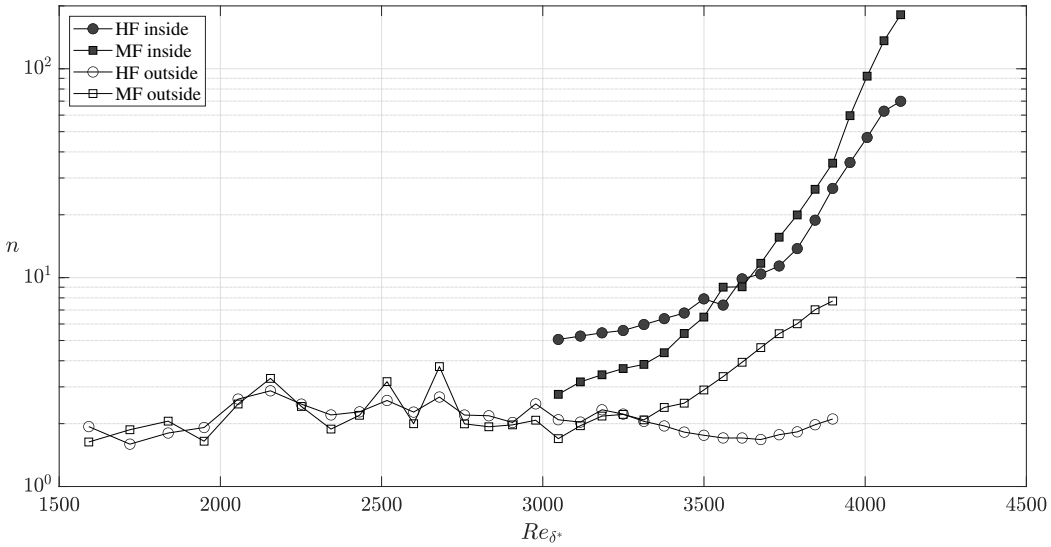

Fig. 7 Stream-wise evolution of fluctuations of the laminar boundary layer.

Measurements outside the boundary layer show that the HF scales have a nearly constant amplitude over the flat plate. As there is no significant amplification and no distinct signature of a coherent scale from the frequency spectrum (Fig. 6), this corresponds to the free-stream noise of the wind tunnel. The amplitude suggests that the noise has a higher level compared to the free-stream, but constant nonetheless. The MF scales also exhibit a similar constant amplitude up to $Re_{\delta^*} \approx 3300$, after which they show a steady exponential growth. Measurements made inside the boundary layer show that both time-scales are continuously amplified. The HF scale starts with a higher relative amplitude compared to the MF scale. However, the growth rate of the MF scale is higher than the HF scale. Once the two curves cross, the HF scale grows with the same rate of the MF scale, reaching a relative amplitude of more than 2 decades over the initial value. For context, the broadband turbulence intensity (in terms of mass-flux fluctuations) at the end of the flat plate is 0.21% outside the boundary layer and 5.65% inside the boundary layer. It is also interesting to observe the "dissipation" of the amplitude measured outside the boundary layer relative to what was measured inside. The amplitude of the MF scales outside the boundary layer is approximately half of the value measured inside. It is to be noted that the stream-wise coordinate of the measurements made outside are projected to the wall based on characteristic angles and hence, there should not be an offset based on the location of the sources.

These results suggest that the boundary layer undergoes transition through the growth of two time-scales; the first step involves the growth of self-excited HF modes corresponding to the 3D oblique waves. While these modes dominate the frequency space inside the boundary layer, their presence cannot be detected outside the boundary layer. Once these modes reach a critical amplitude, they trigger the growth of secondary instabilities corresponding to MF stream-wise streak-like structures. The presence of these MF scales indicates the beginning of the non-linear regime of the transition process, resulting in modifications to the mean boundary layer profile, gradually making it more turbulent. Additionally, these MF scales have a higher growth rate compared to the HF scales and their presence can also be detected outside the boundary layer, albeit with lower amplitude.

Thus, a critical Reynolds number can be determined based on the location where the secondary instabilities are first observed outside the boundary layer. This value was found to be $Re_{\delta^*} \approx 3314$ or $Re_x \approx 1.4 \times 10^6$ (based on the stream-wise coordinate). This critical value denotes the beginning of the transition process. The location where a fully turbulent profile can be obtained will be further downstream of this critical Reynolds number.

For reference, the location of the corner of the compression ramp expressed in terms of this Reynolds number is $Re_{\delta^*} = 3117$. Thus, the location of the corner is in the part of the boundary layer where the profile is still fully laminar (Fig. 5) and the secondary instabilities are not "yet" dominant inside the boundary layer (Fig. 6). This ensures that the compression ramp interacts with a canonical laminar boundary layer and not one that has begun the transition process.

B. Shock-wave Boundary Layer Interaction (SBLI)

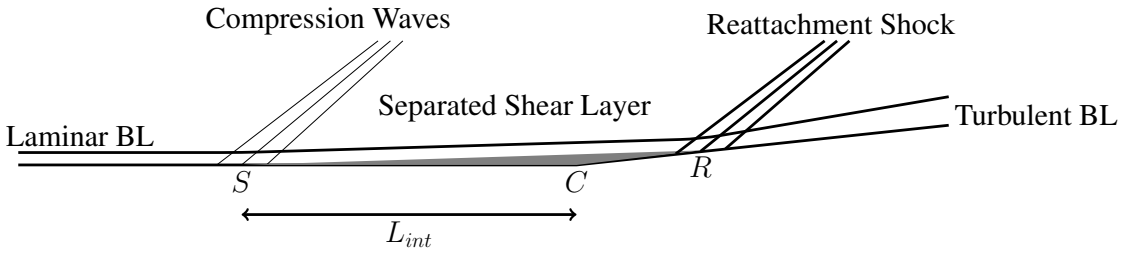

Fig. 8 Illustration of the SBLI over the compression ramp.

The interaction between the laminar boundary layer and the compression ramp is illustrated in Fig. 8, where the points S, C and R represent separation, corner of ramp and reattachment of the boundary layer respectively. Separation is characterized by weak compression waves and a stronger flow deflection at reattachment leads to a coalescing of compression waves into a shock-wave further away from the wall. The recirculating region is long and thin, shown by the gray region between the points S, C and R. Such large aspect ratios of the separated region was also found by previous studies [24, 26, 28]. Far downstream of reattachment, the boundary layer is expected to be fully turbulent. Revisiting the topic of critical Reynolds number from the previous section, given the large aspect ratio of the separated region, Reynolds number at separation would be a better parameter to estimate the state of the boundary layer upstream of the interaction. Reynolds number at separation of the boundary layer was found to be $Re_{\delta^*} = 2888$, which is clearly upstream of the critical Reynolds number estimated in the previous section.

Figure 9 shows the external longitudinal measurements from the Pitot probe, which are made a constant height of 5 mm above the wall. The stream-wise coordinate is expressed in non-dimensional form with $X^* = 0$ corresponding to the mean location of separation, S and $X^* = 1$ corresponding to the location of the corner, C (Fig. 8). The average location of separation is determined by identifying the peak in the gradient of longitudinal pressure. As the measurements are made at a height of 5 mm from the wall, X^* is determined using projected coordinates, along characteristics. The left vertical axis shows non-dimensional pressure coefficient (c_p) over the interaction, and a two-step pressure rise can be observed, typical of separated SBLIs. The overall pressure rise agrees quite well with the inviscid step (shown by the dashed-dotted line), with a slight underestimation from the experiments, as the total pressure loss across the reattachment shock cannot be accurately determined.

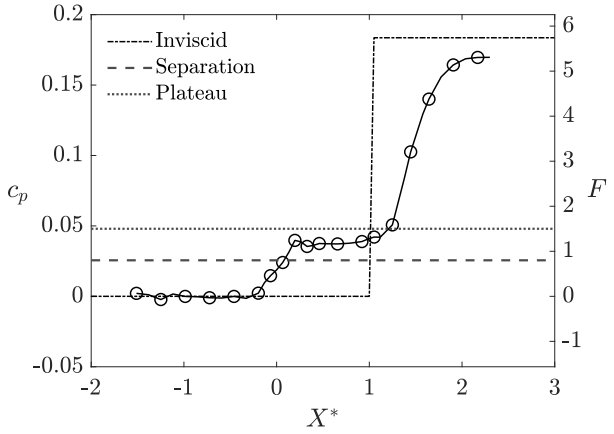

Fig. 9 Stream-wise evolution of non-dimensional pressure over the compression ramp.

The right vertical axis of Fig. 9 shows the pressure measurements expressed in coefficient of free-interaction (F), which takes into account the effect of Mach and Reynolds number (through the skin-friction coefficient (c_f), according to Eq. 4) to provide universal values for separation and plateau pressure of SBLIs [38]. It can be seen that the experimental measurements agree quite well with typical values of separation ($F = 0.8$, indicated by the dashed line) and plateau

pressure ($F = 1.5$, indicated by the dotted line) for laminar separated SBLIs [22]. These results validate the canonical nature of the current SBLI experiments. The length of interaction, L_{int}, defined as the stream-wise distance between the mean location of separation, S and the location of the corner, C (Fig. 8), was measured to be $62\delta^*_s$, where the displacement thickness at separation was taken as reference. A more detailed analyses of the interaction lengths for different Reynolds numbers as well as comparisons with oblique shock reflections have been published by the authors in the proceedings of the Turbulent Shear Flow Phenomenon (TSFP) conference [39].

$$\frac{p - p_0}{q_0} = F(X^*)\sqrt{\frac{2c_f}{\left(M^2 - 1\right)^{(1/2)}}} \tag{4}$$

The frequency space of the hot-wire measurements provide a more detailed outlook on the time-scales of the interaction. External longitudinal explorations by the hot-wire probe are made at a height of 23 mm above the wall, which was chosen to avoid interactions between the probe support system and the ramp geometry. Figure 10 shows the evolution of normalized pre-multiplied PSD over the compression ramp, similar to Fig. 6. Frequency is expressed in non-dimensional Strouhal number, $St_L = fL_{int}/U_\infty$ (where L_{int} is the length of interaction) on the left vertical axis in logarithmic scale. The right vertical axis shows non-dimensional angular frequency expressed according to boundary layer scaling (Eq. 1). The conversion factor between the two non-dimensional frequency scales is $St_L/\omega^* = 3.5 \times 10^{-5}$. The horizontal axis represents the projected non-dimensional stream-wise coordinate (X^*) similar to Fig. 9.

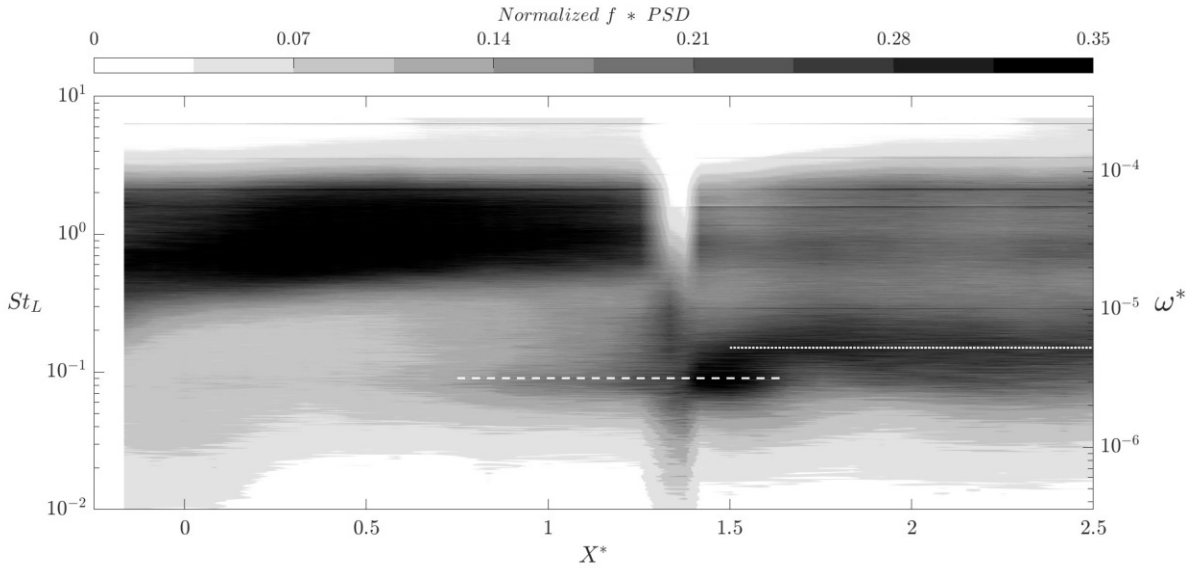

Fig. 10 Longitudinal evolution of normalized pre-multiplied power spectral density over the compression ramp.

The separation bubble ($0 \leq X^* \leq 1$) seems to be dominated by a broad range of high frequency scales centered around $St_L \approx 1$ ($2 \times 10^{-5} \leq \omega^* \leq 1 \times 10^{-4}$). These scales do not seem to be related to the interaction and might be the measurement of high frequency noise of the wind tunnel. Similar noise was measured over the flat plate outside the boundary layer (Fig. 6). This will be further addressed in the following paragraphs.

Reattachment shock can be clearly identified downstream of the corner at $X^* = 1.4$. The shock signal seems to be characterized by a wide range of low frequencies centered around $St_L \approx 0.09$ (indicated by the dashed white line). A signature of this low frequency unsteadiness can also be observed just downstream of reattachment. Surprisingly, this LF scale does not seem to be dominant at the separation of the boundary layer, suggesting that the amplitude of unsteadiness might be quite low. Similar low frequency unsteadiness was found by experimental investigations of transitional oblique shock reflections at similar Mach and Reynolds number conditions [28, 40]. However, numerical simulations found lower Strouhal numbers of $St_L \approx 0.04$ [26, 27]. At higher Mach numbers, experiments on transitional SBLIs over compression ramps found low-frequency unsteadiness at $St_L \approx 0.025$ [41]. This discrepancy remains an open question in the field of transitional SBLIs.

Additionally, an intermediate scale can be seen around $St_L \approx 0.15$ ($\omega^* \approx 6 \times 10^{-6}$) downstream of reattachment,

annotated by the dotted white line. The frequency of these scales are approximately in the same range of frequencies associated with streak-like structures observed over the natural boundary layer (Fig. 6). Recent experimental and numerical studies on transitional compression ramps at low hypersonic speeds, found similar streak-like structures in the boundary layer at reattachment [42]. These time-scales were found to be essential for the breakdown process leading to turbulence [43]. Although the Mach number of these investigations are higher than the current experiments, the transitional mechanisms involved similar amplification of oblique modes and stream-wise streak-like structures. Although these scales are observed after reattachment, no concentration of PSD can be seen at very high frequencies, suggesting the absence of the typical cascade to turbulence. The results from Fig. 11 and 10 suggest that the boundary layer is not fully turbulent at reattachment, but still undergoing transition.

Fig. 11 shows the longitudinal evolution of non-dimensional mass-flux fluctuations over the compression ramp. The amplitude is again expressed according to Eq. 3 and calculated for three time-scales: low frequency (LF) corresponding to the unsteadiness found at reattachment, medium frequency (MF) found downstream of reattachment and high frequency (HF) found over the separation bubble.

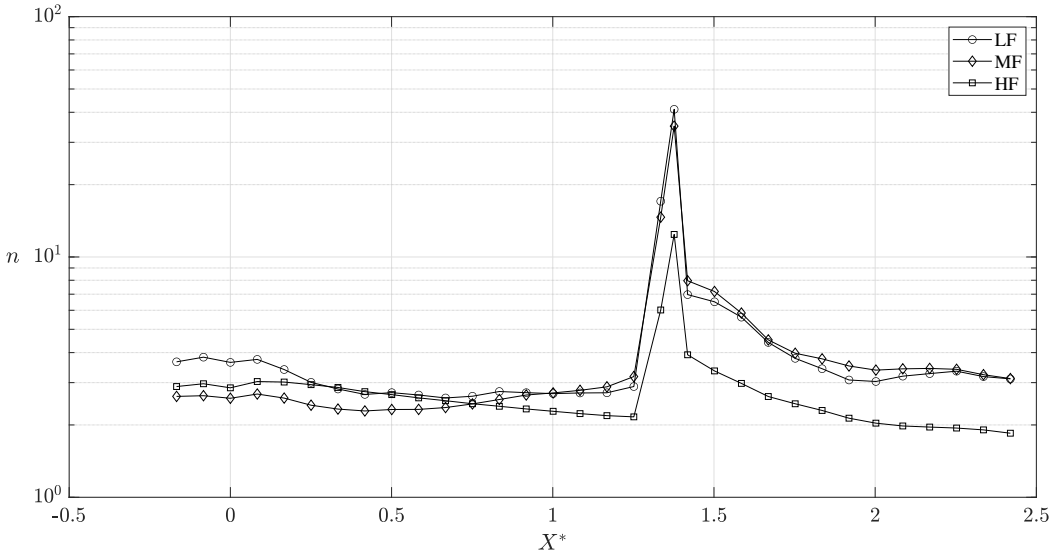

Fig. 11 Longitudinal evolution of non-dimensional fluctuations of mass-flux over the compression ramp.

The three time-scales exhibit a general trend of an overshoot due to the reattachment shock, with subtle differences upstream and downstream. LF seems to be the most dominant at separation ($X^* = 0$) and reaches a lower plateau value till reattachment. MF remains fairly constant up to reattachment with a small increase over the second half of the bubble. Downstream of the reattachment shock, both the LF and MF have a higher amplitude relative to upstream of the interaction, suggesting a localized amplification due to the shock-wave. Their amplitude gradually decreases moving downstream and reaching the initial value found upstream of the interaction. The HF scale shows a decreasing amplitude over the separation bubble and continues to decrease after reattachment, with a relatively lower overshoot (compared to the LF and MF scales), thus confirming that the HF scales observed over the interaction are mostly related to the noise of the wind tunnel.

The overarching theme of these results is the absence of steady exponential growth either before or after reattachment, indicating the absence of canonical transitional mechanisms as seen in Fig. 7. But perhaps the boundary layer undergoes transition in another scenario. As the boundary layer has experienced a strong adverse pressure gradient due to the interaction, the mean velocity profile is expected to be severely decelerated downstream of reattachment and not to follow the shape of canonical boundary layer profiles. Such a velocity profile is not suited for the steady growth of conventional modes or structures associated with natural transition.

In order to shed more light on the state of the boundary layer after reattachment, hot-wire measurements are made inside the boundary layer at various locations downstream of the interaction using the same boundary layer probe shown in Fig. 3b. Figure 12 shows PSD of the hot-wire measurements made inside the boundary layer after reattachment. The PSD is represented in pre-multiplied form without normalization to highlight the evolution of relative

amplitudes between different stream-wise locations. Frequency is shown in logarithmic scale on the horizontal axis, with non-dimensional angular frequency, ω^* (boundary layer normalization) on the bottom and Strouhal number based on the length of interaction, St_L (SBLI normalization) on the top. It is important to note that the measurements made outside the boundary layer have four orders of magnitude lower amplitude compared to the measurements made inside the boundary layer. Further, these results highlight the strong contrast between the frequency scales observed inside and outside the boundary layer.

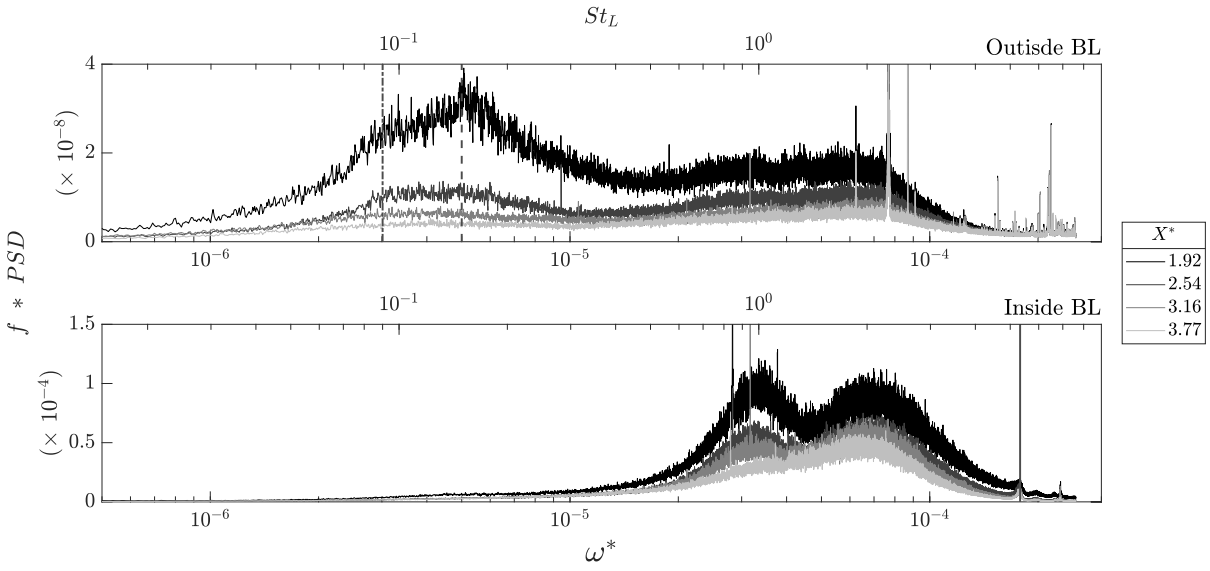

Fig. 12 Pre-multiplied power spectral density downstream of the SBLI.

Outside the boundary layer, most of the energy is concentrated at relatively lower frequencies. Evidence of MF scales are found, represented by the dashed vertical line, similar to Fig. 6 and 10. Additionally, evidence of remnant LF unsteadiness can also be found around $St_L \approx 0.09$, annotated by the dashed-dotted vertical line. Both of these scales decay quite rapidly moving further away from the interaction. No coherent high frequency scales can be identified. The last measurement point, which is nearly four length scales downstream of the interaction, measures very low amplitudes, close to the free-stream noise of the wind tunnel.

Inside the boundary layer, most of the energy is concentrated at higher frequencies. Evidence of boundary layer oblique modes ($2 \times 10^{-5} \leq \omega^* \leq 4 \times 10^{-5}$) can be seen, in the same range as observed from the natural boundary layer measurements (Fig. 6). Also, a very high frequency scale (VHF) can be observed between $5 \times 10^{-5} \leq \omega^* \leq 1 \times 10^{-4}$, which was not found inside the natural boundary layer. The black vertical line at $\omega^* = 1.8 \times 10^{-4}$ represents the theoretical cut-off of the hot-wire anemometer for reference. Moreover, both of these scales reduce in amplitude moving downstream, with the oblique modes decaying faster than the VHF scales. This suggests that the boundary layer is still recovering, up to three interaction lengths downstream of reattachment. On first look, it appears that the MF scales are not found inside the boundary layer. By limiting the vertical axis, MF scales can be identified in the same range of frequencies ($\omega^* \approx 5 \times 10^{-6}$) found in the natural boundary layer (Fig. 13, annotated by the vertical dashed line). The HF and the VHF scale are also shown for reference using the dotted and dashed-dotted line respectively. Comparing Fig. 12 and 13, it can be seen that the amplitude of HF scales are more than one order of magnitude higher than the MF scales inside the reattached boundary layer. Also, the amplitude of these MF scales decay quite rapidly and cannot be observed at the next measurement point. These results suggest an alternate breakdown scenario of laminar boundary layers, bypassing the growth of secondary instabilities.

On the other hand, no evidence of LF unsteadiness can be observed inside the boundary layer (Fig. 13), possibly due to their very low amplitude with respect to the MF, which cannot be resolved by the hot-wire anemometer.

Figure 14 shows the evolution of broadband mass-flux fluctuations (RMS) after reattachment inside and outside the boundary layer. Both measurements tell the story of a relaxing and recovering boundary layer, with the RMS gradually decreasing over large distances. However, the level of RMS measured inside the boundary layer is greater than 1%. Further, the RMS decreases to approximately half of its original value over a distance of four interaction lengths. The

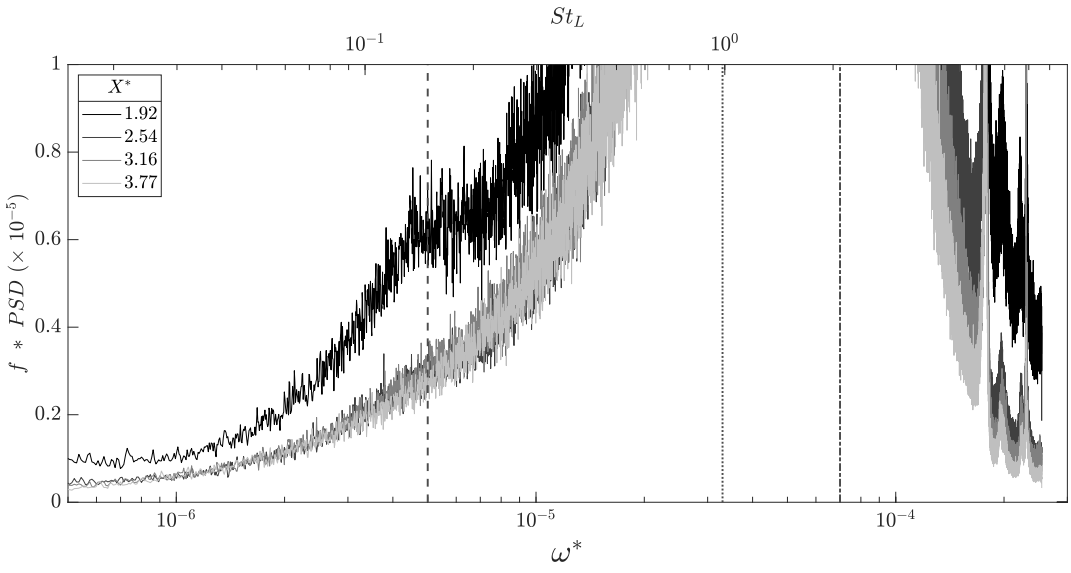

Fig. 13 Pre-multiplied power spectral density inside the boundary layer, downstream of the SBLI.

measurements made outside the boundary layer are analogous to what was seen in Fig. 11, with very low amplitude fluctuations (< 0.1%), close to the free-stream noise of the wind tunnel.

It seems that unlike the transition process of the natural boundary layer, HF oblique modes are the most dominant time-scales inside the boundary layer during the end stages of transition. This is evident by their high amplitude inside the boundary layer downstream of reattachment. Even with such a high amplitude, their presence cannot be detected outside the boundary layer. MF scales are observed inside the boundary layer as well, but having an amplitude one order of magnitude lower than the HF scales. Their existence is apparent by their measurement outside the boundary layer. However, these MF scales are not dominant and decay quite rapidly moving downstream. The presence of new VHF scales imply that the boundary layer is undergoing transition through breakdown of oblique modes, bypassing the rapid growth of MF scales. This transition scenario is clearly different from the natural process over the flat plate.

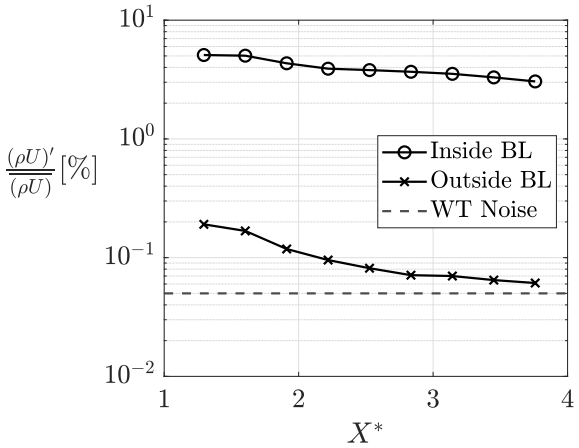

Fig. 14 Non-dimensional fluctuations of mass-flux, downstream of the SBLI.

The current experiments detail the transitional mechanisms over the compression ramp for only one set of Mach and Reynolds numbers. Moreover, the results shown here correspond to a relatively small adverse pressure gradient (i.e. 6° compression ramp). The behavior of these modes when encountered with higher shock strengths cannot be extrapolated

from the current results. Further experiments are required to understand the effects of these flow parameters on these boundary layer time-scales. Moreover, the influence of these transitional modes on the length and time-scales of the SBLI are not fully understood. Parametric studies are necessary to uncover these subtle interdependencies between flow conditions, boundary layer modes and the spatial-temporal organization of transitional SBLIs.

V. Conclusion

Experiments are performed to investigate the transitional mechanisms of supersonic boundary layers. Specifically, comparisons are drawn between the natural transition scenario over a simple flat plate and the altered transition mechanism through shock-wave boundary layer interaction over a compression ramp. The canonical nature of the laminar boundary layer and SBLI has been verified using Pitot probe measurements. Hot-wire anemometer is used to obtain temporal information, including measurements inside boundary layers and over separated shear layers of the SBLI.

It was found that the natural boundary layer undergoes transition in a procedural manner, involving the development of consecutively amplified modes. First the growth of self-excited oblique modes was observed, which in turn triggered the growth of secondary instabilities or stream-wise streak-like structures. Once a critical Reynolds number was reached, these secondary instabilities are amplified exponentially due to non-linear growth, subsequently modifying the mean velocity profile and having large amplitude fluctuations.

Conversely, the boundary layer adopts a different mechanism to undergo transition when interacting with shock-waves. While the same instabilities of the natural transition process are found in the SBLI, their procedural and ordered growth of disturbances are not found. Instead, the boundary layer seems to undergo breakdown of oblique modes, without the rapid growth of secondary instabilities.

These results highlight the subtle contrast in the transitional mechanisms of the laminar boundary layer when interacting with shock-waves. Further experiments and analyses are required to understand the interplay between the influence of flow conditions such as Mach number, Reynolds number and shock strength on the boundary layer transitional modes. Moreover, the consequent effect of these instabilities on the length and time scales of the SBLI require detailed parametric investigations.

Acknowledgments

This work is part of the European TEAMAero project (Towards Effective Flow Control and Mitigation of Shock Effects in Aeronautical Applications). The authors would like to acknowledge the support from the European Union's Horizon 2020 research and innovation programme under grant agreement No. EC grant 860909.

References

[1] Schubauer, G. B., and Skramstad, H. K., "Laminar boundary-layer oscillations and stability of laminar flow," *Journal of the Aeronautical Sciences*, Vol. 14, No. 2, 1947, pp. 69–78.

[2] Benay, R., Chanetz, B., Mangin, B., Vandomme, L., and Perraud, J., "Shock wave/transitional boundary-layer interactions in hypersonic flow," *AIAA journal*, Vol. 44, No. 6, 2006, pp. 1243–1254.

[3] Mack, L. M., "Boundary-layer linear stability theory," Tech. rep., California Inst of Tech Pasadena Jet Propulsion Lab, 1984.

[4] Lees, L., and Lin, C.-C., *Investigation of the stability of the laminar boundary layer in a compressible fluid*, 1115, National Advisory Committee for Aeronautics, 1946.

[5] Laufer, J., and Vrebalovich, T., "Stability and transition of a supersonic laminar boundary layer on an insulated flat plate," *Journal of Fluid Mechanics*, Vol. 9, No. 2, 1960, pp. 257–299.

[6] Kendall, J. M., "Wind tunnel experiments relating to supersonic and hypersonic boundary-layer transition," *AIAA Journal*, Vol. 13, No. 3, 1975, pp. 290–299.

[7] Sandham, N., Adams, N. A., and Kleiser, L., "Direct simulation of breakdown to turbulence following oblique instability waves in a supersonic boundary layer," *Applied scientific research*, Vol. 54, No. 3, 1995, pp. 223–234.

[8] Tollmien, W., "Über die entstehung der turbulenz. nachr. ges. wiss. göttingen 21–24," *English translation NACA TM*, Vol. 609, 1929, p. 1931.

[9] Fasel, H., Thumm, A., and Bestek, H., "Direct numerical simulation of transition in supersonic boundary layers: oblique breakdown," *Fluids Engineering Conference*, Publ by ASME, 1993, pp. 77–92.

[10] Chang, C.-L., and Malik, M. R., "Oblique-mode breakdown and secondary instability in supersonic boundary layers," *Journal of Fluid Mechanics*, Vol. 273, 1994, pp. 323–360.

[11] Shadloo, M., and Hadjadj, A., "Laminar-turbulent transition in supersonic boundary layers with surface heat transfer: a numerical study," *Numerical Heat Transfer, Part A: Applications*, Vol. 72, No. 1, 2017, pp. 40–53.

[12] Mayer, C. S., Von Terzi, D. A., and Fasel, H. F., "Direct numerical simulation of complete transition to turbulence via oblique breakdown at Mach 3," *Journal of Fluid Mechanics*, Vol. 674, 2011, pp. 5–42.

[13] Délery, J., Marvin, J. G., and Reshotko, E., "Shock-wave boundary layer interactions," Tech. rep., Advisory Group for Aerospace Research and Development Neuilly-Sur-Seine (France), 1986.

[14] Dolling, D. S., "Fifty years of shock-wave/boundary-layer interaction research: what next?" *AIAA journal*, Vol. 39, No. 8, 2001, pp. 1517–1531.

[15] Dupont, P., Haddad, C., and Debieve, J., "Space and time organization in a shock-induced separated boundary layer," *Journal of Fluid Mechanics*, Vol. 559, 2006, pp. 255–277.

[16] Souverein, L., Bakker, P., and Dupont, P., "A scaling analysis for turbulent shock-wave/boundary-layer interactions," *Journal of Fluid Mechanics*, Vol. 714, 2013, pp. 505–535.

[17] Erengil, M. E., and Dolling, D. S., "Unsteady wave structure near separation in a Mach 5 compression rampinteraction," *AIAA journal*, Vol. 29, No. 5, 1991, pp. 728–735.

[18] Piponniau, S., Dussauge, J.-P., Debieve, J.-F., and Dupont, P., "A simple model for low-frequency unsteadiness in shock-induced separation," *Journal of Fluid Mechanics*, Vol. 629, 2009, pp. 87–108.

[19] Clemens, N. T., and Narayanaswamy, V., "Low-frequency unsteadiness of shock wave/turbulent boundary layer interactions," *Annual Review of Fluid Mechanics*, Vol. 46, 2014, pp. 469–492.

[20] Touber, E., and Sandham, N. D., "Large-eddy simulation of low-frequency unsteadiness in a turbulent shock-induced separation bubble," *Theoretical and Computational Fluid Dynamics*, Vol. 23, No. 2, 2009, pp. 79–107.

[21] Doerffer, P., Hirsch, C., Dussauge, J.-P., Babinsky, H., and Barakos, G. N., *Unsteady effects of shock wave induced separation*, Vol. 114, Springer Science & Business Media, 2010.

[22] Babinsky, H., and Harvey, J. K., *Shock wave-boundary-layer interactions*, Vol. 32, Cambridge University Press, 2011.

[23] Doerffer, P., Flaszynski, P., Dussauge, J.-P., Babinsky, H., Grothe, P., Petersen, A., and Billard, F., *Transition Location Effect on Shock Wave Boundary Layer Interaction: Experimental and Numerical Findings from the TFAST Project*, Vol. 144, Springer Nature, 2020.

[24] Giepman, R., Schrijer, F., and Van Oudheusden, B., "A parametric study of laminar and transitional oblique shock wave reflections," *Journal of Fluid Mechanics*, Vol. 844, 2018, pp. 187–215.

[25] Diop, M., Piponniau, S., and Pierre, D., "On the length and time scales of a laminar Shock Wave Boundary Layer Interaction," *54th AIAA Aerospace Sciences Meeting*, 2016, p. 0073.

[26] Larchevêque, L., "Low-and Medium-Frequency Unsteadinesses in a Transitional Shock–Boundary Reflection with Separation," *54th AIAA aerospace sciences meeting*, 2016, p. 1833.

[27] Sansica, A., Sandham, N. D., and Hu, Z., "Instability and low-frequency unsteadiness in a shock-induced laminar separation bubble," *Journal of Fluid Mechanics*, Vol. 798, 2016, pp. 5–26.

[28] Diop, M., Piponniau, S., and Dupont, P., "High resolution LDA measurements in transitional oblique shock wave boundary layer interaction," *Experiments in Fluids*, Vol. 60, No. 4, 2019, pp. 1–15.

[29] Van Ingen, J., "The eN method for transition prediction. Historical review of work at TU Delft," *38th Fluid Dynamics Conference and Exhibit*, 2008, p. 3830.

[30] Smits, A. J., and Dussauge, J.-P., *Turbulent shear layers in supersonic flow*, Springer Science & Business Media, 2006.

[31] Diop, M., Piponniau, S., and Dupont, P., "Transition mechanism in a shock wave boundary layer interaction," *Tenth International Symposium on Turbulence and Shear Flow Phenomena*, Begel House Inc., 2017.

[32] Morkovin, M. V., *Fluctuations and hot-wire anemometry in compressible flows*, North Atlantic Treaty Organization advisory Group for aeronautical research, 1956.

[33] Dupont, P., "Etude expérimentale des champs turbulents dans une couche limite supersonique fortement chauffée," Ph.D. thesis, Aix-Marseille 2, 1990.

[34] Kosinov, A., Maslov, A., and Shevelkov, S., "Experiments on the stability of supersonic laminar boundary layers," *Journal of Fluid Mechanics*, Vol. 219, 1990, pp. 621–633.

[35] Demetriades, A., "Growth of disturbances in a laminar boundary layer at Mach 3," *Physics of Fluids A: Fluid Dynamics*, Vol. 1, No. 2, 1989, pp. 312–317.

[36] Teramoto, S., "Large-eddy simulation of transitional boundary layer with impinging shock wave," *AIAA journal*, Vol. 43, No. 11, 2005, pp. 2354–2363.

[37] Giepman, R., Schrijer, F., and Van Oudheusden, B., "High-resolution PIV measurements of a transitional shock wave–boundary layer interaction," *Experiments in Fluids*, Vol. 56, No. 6, 2015, pp. 1–20.

[38] Chapman, D. R., Kuehn, D. M., and Larson, H. K., "Investigation of separated flows in supersonic and subsonic streams with emphasis on the effect of transition," Tech. rep., Ames Aaeronautical Laboratory, NACA-TR-1356., 1958.

[39] Mahalingesh, N., Piponniau, S., and Dupont, P., "Transitional shock-wave boundary layer interaction over a compression ramp," *Twelfth International Symposium on Turbulence and Shear Flow Phenomena (TSFP12)*, 2022.

[40] Bonne, N., Brion, V., Garnier, E., Bur, R., Molton, P., Sipp, D., and Jacquin, L., "Analysis of the two-dimensional dynamics of a Mach 1.6 shock wave/transitional boundary layer interaction using a RANS based resolvent approach," *Journal of Fluid Mechanics*, Vol. 862, 2019, pp. 1166–1202.

[41] Threadgill, J. A., Little, J. C., and Wernz, S. H., "Transitional shock boundary layer interactions on a compression ramp at mach 4," *AIAA journal*, Vol. 59, No. 12, 2021, pp. 4824–4841.

[42] Lugrin, M., Nicolas, F., Severac, N., Tobeli, J.-P., Beneddine, S., Garnier, E., Esquieu, S., and Bur, R., "Transitional shockwave/boundary layer interaction experiments in the R2Ch blowdown wind tunnel," *Experiments in Fluids*, Vol. 63, No. 2, 2022, pp. 1–19.

[43] Lugrin, M., Beneddine, S., Leclercq, C., Garnier, E., and Bur, R., "Transition scenario in hypersonic axisymmetrical compression ramp flow," *Journal of Fluid Mechanics*, Vol. 907, 2021.